

Soliton generation in AlGaAs microresonators at room temperature

Lue Wu,^{1,*} Weiqiang Xie,^{2,*} Chao Xiang,² Lin Chang,² Yan Yu,¹ Hao-Jing Chen,¹
Yoshihisa Yamamoto,³ John E. Bowers,^{2,†} Kerry J. Vahala,^{1,‡} and Myoung-Gyun Suh^{3,§}

¹*T. J. Watson Laboratory of Applied Physics, California Institute of Technology, Pasadena, CA 91125, USA*

²*Department of Electrical and Computer Engineering, University of California,
Santa Barbara, Santa Barbara, California 93106, USA*

³*Physics & Informatics Laboratories, NTT Research, Inc., Sunnyvale, California 94085, USA*

Abstract

Chip-integrated optical frequency combs are attractive optical sources in comb applications requiring high-repetition-rate, low power consumption, or compact size. Spontaneous soliton formation via Kerr parametric oscillation is a promising generation principle in these frequency combs, and has been demonstrated in several material platforms over the past decade. Of these materials, AlGaAs has one of the largest Kerr nonlinearity coefficients allowing low pump threshold comb generation. However, bright soliton generation using this material has only been possible at cryogenic temperature because of the large thermo-optic effect at room temperature, which hinders stable access to the soliton regime. Here, we report self-stabilized single soliton generation in AlGaAs microresonators at room temperature by utilizing a rising soliton step in large free-spectral-range resonators. With sub-milliWatt optical pump power, 1 THz repetition-rate soliton generation is demonstrated. Perfect soliton crystal formation and soliton breather states are also observed. Besides the advantages of large optical nonlinearity, the devices are natural candidates for integration with III-V pump lasers.

Introduction

Optical frequency combs have revolutionized precision time and frequency metrology, and they find a wide range of applications in areas as diverse as spectroscopy, optical communications, distance measurement, and low-noise microwave generation¹. Recent advances in chip-integration of optical frequency combs^{2–5} could accelerate widespread use of frequency combs outside of the laboratory environment. Taking advantage of chip-based high Q-factor microresonators⁶, dissipative Kerr soliton (DKS) formation using the optical $\chi^{(3)}$ nonlinearity is a promising method of comb formation⁷. These soliton microcombs typically feature femtosecond pulse widths and repetition rates ranging from GHz to THz. They are accordingly useful for applications requiring high-repetition-rate, low power consumption, or small form factor. Because the $\chi^{(3)}$ nonlinearity exists in all dielectric materials, DKSs have been demonstrated in many materials including silicon nitride⁸, silica⁹, aluminum nitride¹⁰, and lithium niobate^{11,12}.

Among the various materials, AlGaAs offers a combination of large $\chi^{(3)}$ nonlinearity and high refractive in-

dex for achieving μ W-level Kerr parametric oscillation threshold^{13–17}. Moreover, because of its compatibility with III-V semiconductor lasers, it has the potential to be integrated with pump lasers. However, the large thermo-optical effect of AlGaAs has prohibited soliton generation at room temperature, and either cooling to cryogenic temperature¹⁸ or using generation of dark soliton pulses^{19,20} has been necessary to achieve stable microcombs.

Here, we demonstrate stable room-temperature bright-soliton generation in AlGaAs microresonators for the first time. Single soliton states are generated at repetition rates of 1 THz. The coherence of the resulting soliton microcombs is confirmed by beatnote measurements with a self-referenced fiber comb system, observation of perfect soliton crystals (PSC) with 3 THz repetition rate²¹, and frequency response measurements²². Breather solitons^{23–25} are also observed.

Microresonator Device Characterization

The device was designed using an eigenmode solver with refractive index of $\text{Al}_{0.2}\text{Ga}_{0.8}\text{As}$ taken from the material refractive index database²⁶. Devices with 12.46 μm radius (FSR = 1 THz) and straight bus waveguides were fabricated (photomicrograph in Fig. 1a). Details on the microresonator fabrication are provided in Xie *et al.*¹⁶. A brief summary of the fabrication steps is also included in the Methods section. The fundamental TE mode had a calculated effective index n_{eff} of 2.899, group index n_g of 3.746, and effective mode area A_{eff} of 0.256 μm^2 at 1532 nm, the pumping wavelength in this study.

A tunable ECDL (Toptica CTL1550) was used for both resonator characterization and for pumping of the soliton microcomb. The laser light is coupled in/out the chip bus waveguide through a pair of fiber lenses and pump power is adjusted by a variable optical attenuator (VOA) and monitored before and after the resonator chip by integrating sphere power meters (ISPMs). The ISPMs allowed estimate of the coupling loss to the chip to be 3.3 dB per facet. The bus waveguides were tapered to 200 nm to minimize this loss.

To characterize the mode family dispersion, mode frequencies were measured using the tunable laser with scan wavelength calibrated by an optical spectrum analyzer (OSA). Anomalous dispersion is verified in Fig. 1b where parabolic fitting of the integrated dispersion (i.e., $\omega_\mu - \omega_0 - D_1\mu \approx D_2\mu^2/2$) gives second-order dispersion $D_2/2\pi = 235$ MHz where μ is the mode number relative to pump mode frequency ω_0 , and $D_1/2\pi = 1.013$ THz is

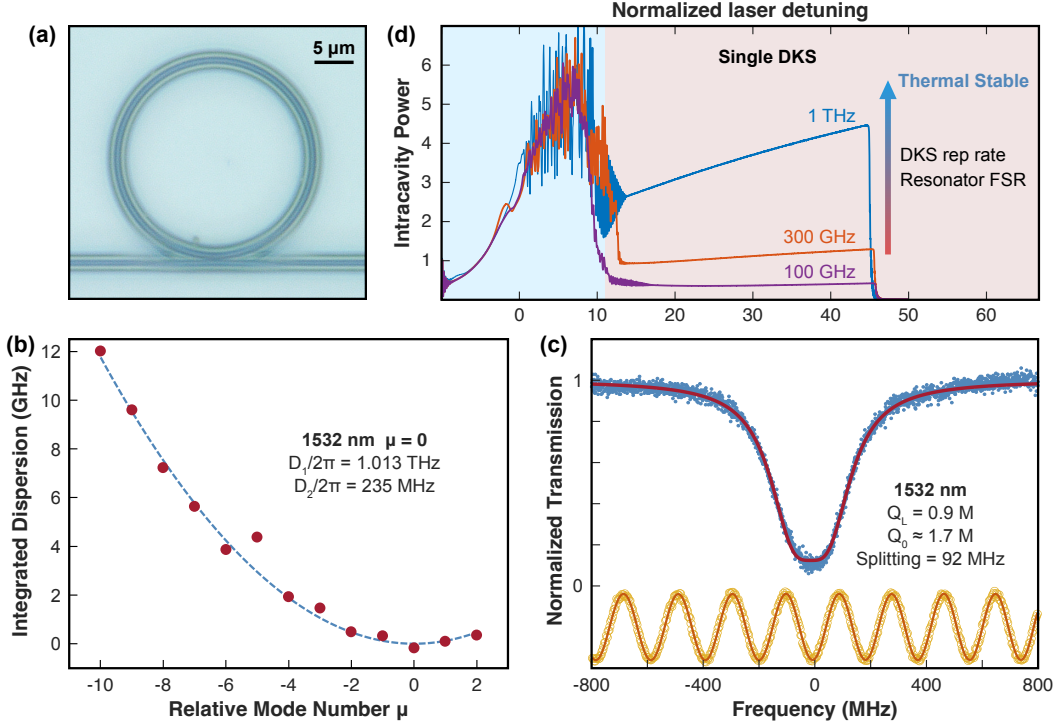


Figure 1. 1 THz FSR AlGaAs microresonator characterization. (a) Optical micrograph of device with radius 12.46 μm . (b) Measured integrated frequency dispersion (red points) is plotted versus the relative mode number, μ . To construct this plot, the center wavelength of each split mode is measured using an OSA and converted to frequency. The mode frequency is given by $\omega_\mu = \omega_0 + \mu D_1 + \frac{1}{2} D_2 \mu^2$, and the blue dashed curve is a fit using $D_1/2\pi = 1.0126$ THz and $D_2/2\pi = 235$ MHz. The measured modes span wavelengths from 1516 to 1620 nm, and $\mu = 0$ corresponds to the pump mode wavelength at 1532 nm. A slight avoided mode crossing near $\mu = -5$ originates from TE/TM mode hybridization. (c) Resonance linewidth measurement of the pumped mode at 1532 nm. Upper trace is the transmission spectrum (blue dots) with a Lorentzian lineshape fitting (red curve) augmented with mode splitting. The full-width-half-maximum (FWHM) linewidth is 210 MHz with splitting of 92 MHz corresponding to an intrinsic $Q_0 = 1.7$ million and loaded $Q_L = 0.92$ M. Lower trace is a frequency calibration (yellow dots) from a fiber Mach-Zehnder Interferometer free spectral range is 191.26 MHz) with sinusoidal fitting (red curve). (d) Numerical simulation of normalized intracavity power versus normalized pump laser detuning ($2\delta\omega/\kappa = 2(\omega - \omega_0)/\kappa$) for three AlGaAs microresonators having FSRs of 100 GHz, 300 GHz and 1 THz. The pump power is set to 36 times parametric oscillation threshold for all three traces. This corresponds to holding the normalized pumping parameter f (see Methods) constant. The parameter D_2/κ is set to the measured value of 1.1 for the 1 THz FSR simulation and scales quadratically with FSR in the other simulations (see Methods for details).

the FSR at the pump frequency. The measured microresonator properties correspond to negative group velocity dispersion (GVD) $\beta_2 = -n_g D_2 / c D_1^2 \approx -455$ ps²/km and $D = -2\pi c \beta_2 / \lambda^2 \approx 366$ ps/nm/km, in good match with the prediction from modeling (346 ps/nm/km). As an aside, the combination of large dispersion and large FSR of this system leads to parametric oscillation initially on the neighboring sidemodes of the pumping mode as observed in microtoroids^{27,28}. Specifically, the peak parametric gain occurs at $\mu - \mu_{\text{pump}} \approx \sqrt{\kappa/D_2} \approx 1$ ⁷.

Intrinsic Q factor $Q_0 = 1.7$ million and loaded Q factor $Q_L = 0.92$ M at the pumping wavelength 1532 nm were measured by characterizing the transmission spectrum as shown in Fig. 1c. The transmission spectrum featured a full-width-half-maximum linewidth of $\kappa/2\pi = 210$ MHz which was broadened slightly by back-scatter-induced splitting of 92 MHz²⁹. In the linewidth measurements,

probe power was maintained low enough to avoid resonance thermal broadening³⁰. The wavelength scan was also performed from blue to red wavelengths so that the measured Q values are conservative.

The threshold for parametric oscillation can be estimated by the following equation^{9,27},

$$P_{\text{th}} = \frac{\pi n_g \omega_0 A_{\text{eff}}}{4\eta n_2} \frac{1}{D_1 Q^2} \quad (1)$$

where n_2 is Kerr nonlinear coefficient, $\eta = Q/Q_{\text{ex}}$ is the waveguide-to-resonator loading factor, and other parameters are given above. Using $n_2 \approx 1.7 \times 10^{-17}$ m²/W³¹, the parametric threshold is estimated to be 20 μW , which agrees well with the measured in-waveguide threshold pump power of 22 μW .

Soliton Generation at Room Temperature

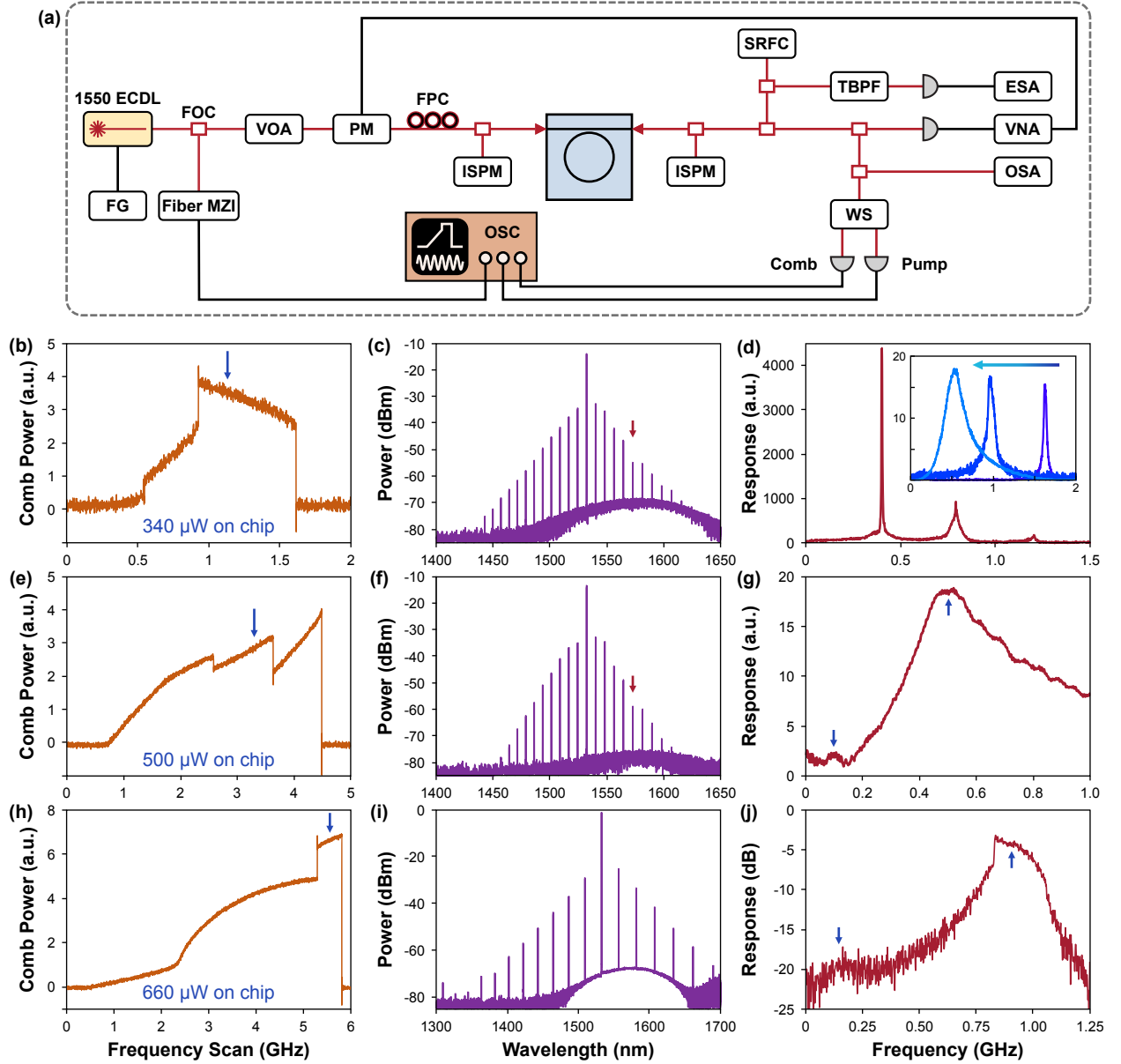


Figure 2. **AlGaAs microresonator soliton generation behavior at different pump power levels.** (a) Experimental setup. FG: Function Generator; ECDL: External Cavity Diode Laser; FOC: Fiber Optic Coupler; Fiber MZI: Fiber Mach-Zehnder Interferometer; VOA: Variable Optical Attenuator; FPC: Fiber Polarization Controller; PM: Phase modulator; VNA: Vector Network Analyzer; WS: Wave Shaper; SRFC: Self-Referenced Fiber Comb; ESA: Electrical Spectral Analyzer; OSA: Optical Spectral Analyzer; OSC: Oscilloscope; ISPM: InGaAs Integrating Sphere Photodiode Power Meter; PD: InGaAs Photodetector; TBPF: Tunable Band-pass Filter. (b)-(d) Breather soliton generation for 300 μW on-chip pump power showing soliton power versus pump frequency scan (b), optical spectrum (c) at scan location given by the blue arrow in (b), and modulation response (d). (a.u. arbitrary units) Note that the $\mu = -5$ comb line (red arrow) is lower as a result of mode crossing (see Fig. 1b). In panel (d) breathing frequency peak and its harmonics are revealed. Inset: frequency response showing C-resonance tuning before tuning into soliton regime. The arrow shows the pump laser scan direction. (e)-(g) Single soliton formation at 500 μW on-chip pump power with content similar to (b)-(d). The blue arrow indicates the single soliton state region and detuning location for spectrum measurement in panel f. In panel (g) the frequency modulation response of the single soliton state shows the S-resonance and C-resonance positions (blue arrows). (h)-(j) 3-FSR perfect soliton crystal formation at 660 μW on-chip pump power. Panels are analogous to (e)-(g).

Room temperature generation of solitons in AlGaAs is frustrated by a combination of large thermo-optic co-

efficient and the abrupt drop of intra-cavity power that usually accompanies soliton formation³². This drop co-

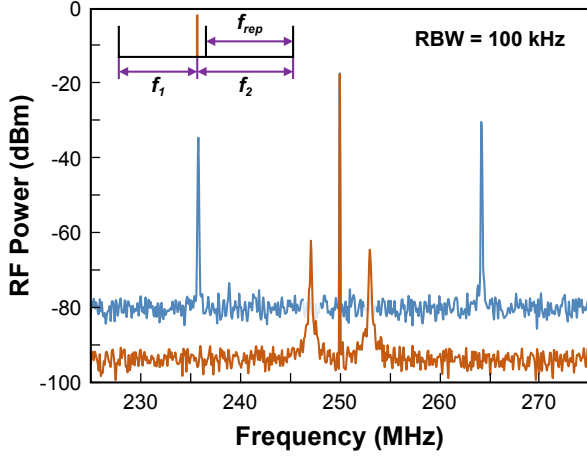


Figure 3. **Single soliton comb line beatnote with self-referenced fiber comb.** The peak at 250 MHz gives the fiber comb repetition rate f_{rep} . In the red trace, the 2 small peaks are beatnotes between the filtered 1548 nm single soliton comb line with 2 fiber comb lines (see inset). The blue trace is the beatnote of the ECDL laser pump line with two fiber comb lines.

incides with the transition of the system from the modulation instability regime to the soliton regime as a pump laser is wavelength tuned from blue to red into the soliton regime. The subsequent rapid cooling of the microresonator mode volume causes its frequency to quickly tune away from the pumping frequency. If the thermo-optic effect is very large, this tuning prevents stable soliton formation. On the other hand, the thermo-optic effect will also self-stabilize an optically pumped system if the intracavity power increases with laser blue-to-red tuning³⁰. For soliton generation, the stability benefit of this increase has been noted in Cole *et al.*³³ and Wang *et al.*³⁴. Specifically, when the soliton power is higher than power emitted in the modulation instability regime, the thermo-optic effect will assist (rather than oppose) stable soliton formation. As illustrated in Fig 1d, this situation can happen when DKSs are operated at very high repetition-rates, which can be arranged by operating a resonator with many co-circulating solitons or by using a large FSR resonator in the single soliton regime.

To demonstrate this effect, the mode at 1532 nm was pumped for soliton generation. Details on the measurement setup are provided in Fig. 2a. A summary of comb behavior at three pump power levels is provided in Fig. 2 b-j. Beginning with panels Fig. 2 b-c, panel b gives the comb power for constant on-chip bus waveguide pump power of 340 μW as the pump laser is scanned in frequency (horizontal axis). A Mach-Zehnder interferometer with a free-spectral-range of 191.26 MHz is used to calibrate the laser frequency scan. The pump line is filtered from the orange comb power trace using a Wave-Shaper. The comb power shows an abrupt power jump where the system transitions from a modulation instabil-

ity (MI) state to a comb state. As discussed earlier, because the comb power is here larger than the MI power, the photothermal effect works to stabilize the system. In fact, it is possible to manually tune the laser frequency into the comb state and stably measure comb spectra^{35,36}. A comb spectrum measured at the detuning indicated by the blue arrow in Fig. 2b is presented in Fig. 2c. The comb line spacing equals one FSR (1 THz, 8 nm). As an aside, the 1572 nm comb line (indicated by the red arrow) is reduced in power as a result of the perturbation to the parabolic dispersion at $\mu = -5$ in Fig. 1b.

To further characterize the comb, phase modulation (PM, Thorlabs LN65S-FC in Fig. 2a) of the pump field was applied in combination with measurement of transmitted power using a vector network analyzer (VNA, Keysight E5061B in Fig. 2a)²². Briefly, the PM is driven by the VNA with RF power of -7 dBm, and the drive frequency is scanned over the span of 1 MHz-3 GHz. Then, the transmitted light through the bus waveguide is detected by a fast photo detector (Thorlabs DXM30AF). The photodetector (PD) output signal is then input to the VNA for analysis. The measurement was repeated at each pumping power level and the resulting spectra are shown in Fig. 2d,g,j.

The measured frequency response spectra in Fig. 2d reveals this comb to correspond to a breather soliton²³⁻²⁵. Specifically, a sharp peak at breathing frequency 400 MHz²⁴ is present with its 2nd and 3rd harmonic overtones. It is noted that modulation is not necessary for the peaks to appear, as the same peaks are observed in the base-band intensity noise spectrum. The soliton breathing frequency could be tuned from 290 MHz to 1 GHz by adjusting the pump-resonance detuning frequency.

By increasing pump power to 500 μW on chip, a single soliton state was measured as shown in Figs. 2e-g. Manual tuning of the pump frequency was again used here. As can be seen in Fig. 2e, the comb step initially decreases slightly but eventually rises above the MI power so that once again the thermo-optic effect helps to stabilize the comb operating point. A comb spectrum is shown in Fig. 2f corresponding to the frequency position given by the arrow in Fig. 2e. The VNA measurement is shown in Fig. 2g. The small spectral bump near 100 MHz is identified as the S-resonance²². The C-resonance at 490 MHz is also apparent for this state.

In Figs. 2h-j, the same measurements are repeated for 660 μW on chip pumping power. Here, the optical spectrum in Fig. 2i reveals that the state is a perfect soliton crystal state^{21,33,37} with its repetition rate equal to 3 FSRs (3 THz, 24 nm) corresponding to three soliton pulses circulating in the cavity. The comb spectrum is spectrally broad spanning 400 nm (1300-1700 nm). Importantly, the ability to observe a soliton crystal further confirms the coherence of the soliton pulses in this system, since this is required to form the 3 FSR comb from coherent interference of three underlying 1 FSR combs.

To further confirm microcomb formation in the sin-

gle soliton state, one of the comb lines (1548 nm line in Fig. 2f, $\mu = -2$) is filtered out and beat with a self-referenced³⁸ fiber comb (Menlo FC1500-250-ULN, $f_{\text{rep}}=250$ MHz and carrier-envelope-offset frequency $f_{\text{CEO}} = 35$ MHz). The beatnote between microcomb and fiber comb is shown in Fig. 3 as the red trace. The strong peak is the fiber comb repetition rate, while the neighboring weaker peaks are beatnotes produced by two fiber comb teeth with the filtered THz comb tooth. The beatnote peak at 247.1 MHz has a full width at half maximum linewidth of 59 kHz, which is an order-of-magnitude narrower than in previous work at 4K temperature¹⁸. For comparison, the beatnote between the pump laser (Toptica ECDL) and the fiber comb is also plotted as the blue trace. The microcomb beatnote is visibly wider than the pump laser beatnote. The specific source of noise in this system is not known, but could be related to pump frequency transduction noise which is known to impact comb repetition rate in other systems^{39,40}. Such repetition rate noise is multiplied with increasing comb tooth number away from the pumping line⁴¹.

As an aside, on account of the THz repetition rate, it was difficult to directly detect the comb rate⁴². Likewise, autocorrelation measurements were difficult due to the sub femto Joule pulse energy. Also, amplification of

the pulses was challenging due to the limited bandwidth of erbium fiber amplifiers in comparison to the soliton spectrum.

Summary and Discussion

We have demonstrated soliton generation in AlGaAs microresonators at room temperature for the first time. In the experiment, we used large FSR resonators to create rising soliton steps and leverage the previously-reported large thermo-optical effect. Low-noise 1 THz repetition-rate soliton generation was possible with only sub-milliwatt optical pump power. Combined with on-chip optical amplifiers⁴³, such a high repetition-rate optical pulse source can be useful in applications such as pulse driven optical computation^{44,45} (e.g. coherent Ising machine^{46–48}) and for THz wave generation⁴². It should also be possible to integrate these devices with III-V pump lasers.

Acknowledgments:

The authors acknowledge Chengying Bao (THU), Maxim Karpov (Enlightra) and Qifan Yang (PKU) for fruitful discussions. A portion of this work was performed in the UCSB Nanofabrication Facility, an open access laboratory.

Author Information:

Weiqiang Xie's current address is Department of Electronic Engineering, Shanghai Jiao Tong University, 800 Dongchuan Road, Shanghai, 200240, China.

* These authors contributed equally to this work.

† bowers@ece.ucsb.edu

‡ vahala@caltech.edu

§ myoung-gyun.suh@ntt-research.com

¹ S. A. Diddams, K. Vahala, and T. Udem, Optical frequency combs: Coherently uniting the electromagnetic spectrum, *Science* **369** (2020).

² A. L. Gaeta, M. Lipson, and T. J. Kippenberg, Photonic-chip-based frequency combs, *Nature Photonics* **13**, 158 (2019).

³ M. Zhang, B. Buscaino, C. Wang, A. Shams-Ansari, C. Reimer, R. Zhu, J. M. Kahn, and M. Lončar, Broad-band electro-optic frequency comb generation in a lithium niobate microring resonator, *Nature* **568**, 373 (2019).

⁴ C. Xiang, J. Liu, J. Guo, L. Chang, R. N. Wang, W. Weng, J. Peters, W. Xie, Z. Zhang, J. Riemensberger, J. Selvidge, T. J. Kippenberg, and J. E. Bowers, Laser soliton microcombs heterogeneously integrated on silicon, *Science* **373**, 99 (2021).

⁵ L. Chang, S. Liu, and J. E. Bowers, Integrated optical frequency comb technologies, *Nature Photonics* **16**, 95 (2022).

⁶ K. J. Vahala, Optical microcavities, *Nature* **424**, 839 (2003).

⁷ T. J. Kippenberg, A. L. Gaeta, M. Lipson, and M. L. Gorodetsky, Dissipative Kerr solitons in optical microresonators, *Science* **361**, eaan8083 (2018).

⁸ V. Brasch, M. Geiselmann, T. Herr, G. Lihachev, M. H. Pfeiffer, M. L. Gorodetsky, and T. J. Kippenberg, Photonic chip-based optical frequency comb using soliton Cherenkov radiation, *Science* **351**, 357 (2016).

⁹ X. Yi, Q.-F. Yang, K. Y. Yang, M.-G. Suh, and K. Vahala, Soliton frequency comb at microwave rates in a high-Q silica microresonator, *Optica* **2**, 1078 (2015).

¹⁰ X. Liu, Z. Gong, A. W. Bruch, J. B. Surya, J. Lu, and H. X. Tang, Aluminum nitride nanophotonics for beyond-octave soliton microcomb generation and self-referencing, *Nature Communications* **12**, 1 (2021).

¹¹ Y. He, Q.-F. Yang, J. Ling, R. Luo, H. Liang, M. Li, B. Shen, H. Wang, K. Vahala, and Q. Lin, Self-starting bi-chromatic LiNbO₃ soliton microcomb, *Optica* **6**, 1138 (2019).

¹² Z. Gong, X. Liu, Y. Xu, and H. X. Tang, Near-octave lithium niobate soliton microcomb, *Optica* **7**, 1275 (2020).

¹³ D. J. Moss, R. Morandotti, A. L. Gaeta, and M. Lipson, New CMOS-compatible platforms based on silicon nitride and Hydex for nonlinear optics, *Nature Photonics* **7**, 597 (2013).

¹⁴ M. Pu, L. Ottaviano, E. Semenova, and K. Yvind, Efficient frequency comb generation in AlGaAs-on-insulator, *Optica* **3**, 823 (2016).

¹⁵ L. Chang, W. Xie, H. Shu, Q.-F. Yang, B. Shen, A. Boes, J. D. Peters, W. Jin, C. Xiang, S. Liu, G. Moille, S.-P. Yu, X. Wang, K. Srinivasan, S. B. Papp, K. Vahala, and J. E. Bowers, Ultra-efficient frequency comb generation in AlGaAs-on-insulator microresonators, *Nature Communications* **11**, 1331 (2020).

¹⁶ W. Xie, L. Chang, H. Shu, J. C. Norman, J. D. Peters, X. Wang, and J. E. Bowers, Ultrahigh-Q AlGaAs-on-insulator microresonators for integrated nonlinear photonics, *Opt. Express* **28**, 32894 (2020).

- ¹⁷ W. Xie, C. Xiang, L. Chang, W. Jin, J. Peters, and J. E. Bowers, Silicon-integrated nonlinear III-V photonics, *Photon. Res.* **10**, 535 (2022).
- ¹⁸ G. Moille, L. Chang, W. Xie, A. Rao, X. Lu, M. Davanco, J. E. Bowers, and K. Srinivasan, Dissipative Kerr Solitons in a III-V Microresonator, *Laser & Photonics Reviews* **14**, 2000022 (2020).
- ¹⁹ H. Shu, L. Chang, Y. Tao, B. Shen, W. Xie, M. Jin, A. Netherton, Z. Tao, X. Zhang, R. Chen, *et al.*, Microcomb-driven silicon photonic systems, *Nature* **605**, 457 (2022).
- ²⁰ H. Shu, L. Chang, C. Lao, B. Shen, W. Xie, X. Zhang, M. Jin, Y. Tao, R. Chen, Z. Tao, S. Yu, Q.-F. Yang, X. Wang, and J. E. Bowers, Sub-milliwatt, widely-tunable coherent microcomb generation with feedback-free operation, *arXiv* **2112.08904** (2021).
- ²¹ M. Karpov, M. H. P. Pfeiffer, H. Guo, W. Weng, J. Liu, and T. J. Kippenberg, Dynamics of soliton crystals in optical microresonators, *Nature Physics* **15**, 1071 (2019).
- ²² H. Guo, M. Karpov, E. Lucas, A. Kordts, M. H. Pfeiffer, V. Brasch, G. Lihachev, V. E. Lobanov, M. L. Gorodetsky, and T. J. Kippenberg, Universal dynamics and deterministic switching of dissipative Kerr solitons in optical microresonators, *Nature Physics* **13**, 94 (2017).
- ²³ C. Bao, J. A. Jaramillo-Villegas, Y. Xuan, D. E. Leaird, M. Qi, and A. M. Weiner, Observation of Fermi-Pasta-Ulam Recurrence Induced by Breather Solitons in an Optical Microresonator, *Phys. Rev. Lett.* **117**, 163901 (2016).
- ²⁴ E. Lucas, M. Karpov, H. Guo, M. Gorodetsky, and T. J. Kippenberg, Breathing dissipative solitons in optical microresonators, *Nature Communications* **8**, 1 (2017).
- ²⁵ M. Yu, J. K. Jang, Y. Okawachi, A. G. Griffith, K. Luke, S. A. Miller, X. Ji, M. Lipson, and A. L. Gaeta, Breather soliton dynamics in microresonators, *Nature Communications* **8**, 1 (2017).
- ²⁶ M. Guden and J. Piprek, Material parameters of quaternary III - V semiconductors for multilayer mirrors at wavelength, *Modelling and Simulation in Materials Science and Engineering* **4**, 349 (1996).
- ²⁷ T. J. Kippenberg, S. M. Spillane, and K. J. Vahala, Kerr-Nonlinearity Optical Parametric Oscillation in an Ultrahigh-Q Toroid Microcavity, *Phys. Rev. Lett.* **93**, 083904 (2004).
- ²⁸ P. Del'Haye, A. Schliesser, O. Arcizet, T. Wilken, R. Holzwarth, and T. J. Kippenberg, Optical frequency comb generation from a monolithic microresonator, *Nature* **450**, 1214 (2007).
- ²⁹ T. J. Kippenberg, S. M. Spillane, and K. J. Vahala, Modal coupling in traveling-wave resonators, *Opt. Lett.* **27**, 1669 (2002).
- ³⁰ T. Carmon, L. Yang, and K. J. Vahala, Dynamical thermal behavior and thermal self-stability of microcavities, *Opt. Express* **12**, 4742 (2004).
- ³¹ M. Gao, Q.-F. Yang, Q.-X. Ji, H. Wang, L. Wu, B. Shen, J. Liu, G. Huang, L. Chang, W. Xie, *et al.*, Probing material absorption and optical nonlinearity of integrated photonic materials, *Nature Communications* **13**, 1 (2022).
- ³² T. Herr, V. Brasch, J. D. Jost, C. Y. Wang, N. M. Kondratiev, M. L. Gorodetsky, and T. J. Kippenberg, Temporal solitons in optical microresonators, *Nature Photonics* **8**, 145 (2014).
- ³³ D. C. Cole, E. S. Lamb, P. Del'Haye, S. A. Diddams, and S. B. Papp, Soliton crystals in Kerr resonators, *Nature Photonics* **11**, 671 (2017).
- ³⁴ W. Wang, Z. Lu, W. Zhang, S. T. Chu, B. E. Little, L. Wang, X. Xie, M. Liu, Q. Yang, L. Wang, J. Zhao, G. Wang, Q. Sun, Y. Liu, Y. Wang, and W. Zhao, Robust soliton crystals in a thermally controlled microresonator, *Optics Letters* **43**, 2002 (2018).
- ³⁵ Q. Li, T. C. Briles, D. A. Westly, T. E. Drake, J. R. Stone, B. R. Ilic, S. A. Diddams, S. B. Papp, and K. Srinivasan, Stably accessing octave-spanning microresonator frequency combs in the soliton regime, *Optica* **4**, 193 (2017).
- ³⁶ M. H. P. Pfeiffer, C. Herkommer, J. Liu, H. Guo, M. Karpov, E. Lucas, M. Zervas, and T. J. Kippenberg, Octave-spanning dissipative Kerr soliton frequency combs in Si₃N₄ microresonators, *Optica* **4**, 684 (2017).
- ³⁷ Z. Lu, H.-J. Chen, W. Wang, L. Yao, Y. Wang, Y. Yu, B. Little, S. Chu, Q. Gong, W. Zhao, *et al.*, Synthesized soliton crystals, *Nature Communications* **12**, 1 (2021).
- ³⁸ D. J. Jones, S. A. Diddams, J. K. Ranka, A. Stentz, R. S. Windeler, J. L. Hall, and S. T. Cundiff, Carrier-envelope phase control of femtosecond mode-locked lasers and direct optical frequency synthesis, *Science* **288**, 635 (2000).
- ³⁹ X. Yi, Q.-F. Yang, X. Zhang, K. Y. Yang, X. Li, and K. Vahala, Single-mode dispersive waves and soliton microcomb dynamics, *Nature Communications* **8**, 1 (2017).
- ⁴⁰ Q.-F. Yang, Q.-X. Ji, L. Wu, B. Shen, H. Wang, C. Bao, Z. Yuan, and K. Vahala, Dispersive-wave induced noise limits in miniature soliton microwave sources, *Nature Communications* **12**, 1 (2021).
- ⁴¹ F. Lei, Z. Ye, Ö. B. Helgason, A. Fülöp, M. Girardi, and V. Torres-Company, Optical linewidth of soliton microcombs, *Nature Communications* **13**, 1 (2022).
- ⁴² S. Zhang, J. M. Silver, X. Shang, L. D. Bino, N. M. Ridler, and P. Del'Haye, Terahertz wave generation using a soliton microcomb, *Opt. Express* **27**, 35257 (2019).
- ⁴³ Y. Liu, Z. Qiu, X. Ji, J. He, J. Riemensberger, M. Hafermann, R. N. Wang, J. Liu, C. Ronning, and T. J. Kippenberg, A photonic integrated circuit based erbium-doped amplifier, *Science* **376**, 1309 (2022).
- ⁴⁴ I. L. Markov, Limits on fundamental limits to computation, *Nature* **512**, 147 (2014).
- ⁴⁵ J. Feldmann, N. Youngblood, C. D. Wright, H. Bhaskaran, and W. H. Pernice, All-optical spiking neurosynaptic networks with self-learning capabilities, *Nature* **569**, 208 (2019).
- ⁴⁶ Y. Yamamoto, T. Leleu, S. Ganguli, and H. Mabuchi, Coherent Ising machines—Quantum optics and neural network Perspectives, *Applied Physics Letters* **117**, 160501 (2020).
- ⁴⁷ P. L. McMahon, A. Marandi, Y. Haribara, R. Hamerly, C. Langrock, S. Tamate, T. Inagaki, H. Takesue, S. Utsunomiya, K. Aihara, *et al.*, A fully programmable 100-spin coherent Ising machine with all-to-all connections, *Science* **354**, 614 (2016).
- ⁴⁸ T. Honjo, T. Sonobe, K. Inaba, T. Inagaki, T. Ikuta, Y. Yamada, T. Kazama, K. Enbutsu, T. Umeki, R. Kasahara, K. ichi Kwarabayashi, and H. Takesue, 100,000-spin coherent Ising machine, *Science Advances* **7**, eabh0952 (2021).
- ⁴⁹ L. A. Lugiato and R. Lefever, Spatial Dissipative Structures in Passive Optical Systems, *Phys. Rev. Lett.* **58**, 2209 (1987).
- ⁵⁰ X. Yi, *Physics and applications of microresonator solitons and electro-optic frequency combs*, *Ph.D. thesis*, California Institute of Technology (2017).

Methods

Device fabrication

The $\text{Al}_{0.2}\text{Ga}_{0.8}\text{As}$ was grown by molecular beam epitaxial (MBE) on a 3 inch GaAs substrate, which was then bonded to a 3 μm thick thermal oxide layer grown on a 4 inch Si substrate by thermal oxidation. The GaAs substrate was subsequently removed by the etch-stop layer technique using a 500 nm $\text{Al}_{0.8}\text{Ga}_{0.2}\text{As}$ layer. A 100 nm thick SiO_2 layer was deposited using atomic layer deposition (ALD) as a dry etch hard mask. The microresonator pattern was generated by deep-ultraviolet (DUV) photolithography (248 nm). The photoresist after development was then reflowed at 155°C to reduce pattern line edge roughness (LER)¹⁶. The pattern was transferred to the SiO_2 hard mask by inductively coupled plasma reactive-ion etching (ICP-RIE) with a mixture of $\text{CHF}_3/\text{CF}_4/\text{O}_2$. The $\text{Al}_{0.2}\text{Ga}_{0.8}\text{As}$ was then etched through by ICP-RIE with a mixture of Cl_2/N_2 having high etching selectivity (>10 selectivity of AlGaAs over SiO_2) to make the vertical sidewall. Surface passivation of the AlGaAs waveguides was implemented by depositing a 5-10 nm Al_2O_3 layer and a 50-nm SiO_2 layer using ALD. The passivation reduces absorption caused by surface states. The wafer was then cladded with 1.5 μm thick SiO_2 using plasma-enhanced chemical vapor deposition (PECVD) and diced into device chips with dicing saw line aligned with the 200 nm waveguide tapering region to enable low facet coupling loss.

Numerical Simulations

The slowly varying (slower than the round trip) intracavity field $A(\phi, t)$ in the microresonator can be described by Lugiato-Lefever equation (LLE)⁴⁹:

$$\frac{\partial A}{\partial t} = -\left(\frac{\kappa}{2} + i\delta\omega\right)A + i\frac{D_2}{2}\frac{\partial^2 A}{\partial \phi^2} + ig|A|^2A + \sqrt{\frac{\kappa\eta P_{\text{in}}}{\hbar\omega_0}} \quad (2)$$

where $g = \hbar\omega_0^2 n_2 D_1 / 2\pi n_g A_{\text{eff}}$ denotes the normalized Kerr effect nonlinear coefficient, t is the slow time, ϕ is the angular coordinate in the ring resonator in a frame

copropagating with the soliton, κ is the cavity total loss rate, $\delta\omega = \omega - \omega_0$ is the pump cavity detuning (ω is the pump laser frequency and ω_0 is the cavity resonance frequency), D_2 is the cavity group velocity dispersion (GVD), $\eta = \kappa_{\text{ex}}/\kappa$ is the cavity coupling factor (i.e., waveguide coupling rate κ_{ex} normalized to total loss rate κ), and \hbar is the reduced Planck constant. The thermo-optical effect and mode splitting are not included in this equation.

To generate Fig. 1b in the main text, the resonator diameter is varied to obtain resonator FSR ($D_1/2\pi$) values of 100 GHz, 300 GHz and 1 THz. The resonator intrinsic loss (κ_{in}) and loading (η) are fixed so that the total loss (κ) is fixed. The resonator transverse mode properties (A_{eff} , n_g and β_2) are also fixed. However, since the group velocity dispersion $\beta_2 = -n_g D_2 / c D_1^2$ (GVD) is constant, D_2 scales quadratically with D_1 . Also, the parametric oscillation threshold P_{th} scales inversely with D_1 . Therefore, in plotting Fig. 1b, we have set the input pump power P_{in} to scale inversely with D_1 . This has the effect of holding the normalized pumping parameter f (see below) constant as D_1 is varied. It also maintains a constant soliton step length in the plots since the soliton existence range depends upon f .

For numerical simulation, it is convenient to normalize the LLE equation^{7,50} by taking $\tau = t \cdot \kappa/2$ and $\Psi = \sqrt{2g/\kappa}A$, where τ is normalized time, and $\Psi(\phi, \tau)$ is the normalized slowing varying optical field, the following equation results,

$$\frac{\partial \Psi}{\partial \tau} = -(1 + i\zeta)\Psi + i\frac{D_2}{\kappa}\frac{\partial^2 \Psi}{\partial \phi^2} + i|\Psi|^2\Psi + f \quad (3)$$

where $\zeta = 2\delta\omega/\kappa$ is the normalized cavity detuning and $f = \sqrt{8\eta g P_{\text{in}}/\kappa^2 \hbar\omega_0}$ is the normalized pumping term that, as noted above, is held constant as D_1 is varied. Also, ϕ remains the angular coordinate after normalization. Since f is held constant, only D_2/κ in Eq.3 determines the system behavior. Again, D_2 scales quadratically with D_1 for constant GVD and produces different behaviors in simulation presented in Fig. 1b.